JGR Planets

RESEARCH ARTICLE
10.1029/2020JE006540

Special Section:
InSight at Mars

The Seismic Moment and Seismic Efficiency of Small Impacts on Mars

N. Wójcicka[1], G. S. Collins[1], I. D. Bastow[1], N. A. Teanby[2], K. Miljković[3], A. Rajšić[3], I. Daubar[4], and P. Lognonné[5]

[1]Department of Earth Science and Engineering, Imperial College, London, UK, [2]School of Earth Sciences, University of Bristol, Bristol, UK, [3]School of Earth and Planetary Sciences, Curtin University, Perth, Western Australia, Australia, [4]Department of Earth, Environmental and Planetary Sciences, Brown University, Providence, RI, USA, [5]Université de Paris, Institut de physique du globe de Paris, CNRS, Paris, France

Abstract Since landing in late 2018, the InSight lander has been recording seismic signals on the surface of Mars. Despite nominal prelanding estimates of one to three meteorite impacts detected per Earth year, none have yet been identified seismically. To inform revised detectability estimates, we simulated numerically a suite of small impacts onto Martian regolith and characterized their seismic source properties. For the impactor size and velocity range most relevant for InSight, crater diameters are 1–30 m. We found that in this range scalar seismic moment is 10^6–10^{10} Nm and increases almost linearly with impact momentum. The ratio of horizontal to vertical seismic moment tensor components is ~1, implying an almost isotropic *P* wave source, for vertical impacts. Seismic efficiencies are ~10^{-6}, dependent on the target crushing strength and impact velocity. Our predictions of relatively low seismic efficiency and seismic moment suggest that meteorite impact detectability on Mars is lower than previously assumed. Detection chances are best for impacts forming craters of diameter >10 m.

Plain Language Summary NASA's InSight lander has been recording signals, including ground vibrations, on the surface of Mars since early 2019. On Earth, seismologists routinely study earthquakes, but equivalent disturbances on Mars, marsquakes, are not expected to be as large in magnitude. Meteorite impacts were therefore expected to provide another valuable source of seismic energy on Mars, but none have been detected so far. Our understanding of how efficiently meteorites of a given size generate seismic energy therefore requires revision. Using a suite of numerical simulations replicating small impacts on Mars, we conclude that both the magnitude of seismic vibrations and the proportion of the meteorite's kinetic energy that is transferred into distant ground motions are below previous estimates. Small meteorite impacts thus produce smaller and less energetic disturbances than previously predicted, which partially explains lack of detected impacts by InSight. Our results show that the best opportunity of detection is offered by impacts forming craters larger than 10 m in diameter.

Key Points:
- Numerical simulations of small impacts on Mars show that scalar seismic moment is proportional to impact momentum
- Seismic efficiency is ~10^{-6}, comparable with that measured for artificial impacts on the Moon
- InSight's impact detection chances are best for impacts forming craters of diameter >10 m

Supporting Information:
- Supporting Information S1

Correspondence to:
N. Wójcicka,
n.wojcicka18@imperial.ac.uk

Citation:
Wójcicka, N., Collins, G. S., Bastow, I. D., Teanby, N. A., Miljković, K., Rajšić, A., et al. (2020). The seismic moment and seismic efficiency of small impacts on Mars. *Journal of Geophysical Research: Planets*, *125*, e2020JE006540. https://doi.org/10.1029/2020JE006540

Received 29 MAY 2020
Accepted 17 SEP 2020
Accepted article online 25 SEP 2020

1. Introduction

Since early 2019, the InSight (Interior Exploration using Seismic Investigations, Geodesy and Heat Transport) lander has been measuring seismic signals on Mars. By September 2019, it had detected 174 marsquakes, providing the first measurements of Martian seismicity (Banerdt et al., 2020). InSight's seismometer is outperforming its design requirements, with a lower noise floor than any previous seismometer deployed on a terrestrial body (Lognonné et al., 2020). However, no InSight signals have been unequivocally attributed to meteorite impacts (Banerdt et al., 2020; Giardini et al., 2020). Nominal prelanding predictions estimated that in one Martian year between a few and tens of small impacts (forming craters of diameter 0.5–20 m) would be detectable by InSight, the majority of which would be occurring on a regional scale (Daubar et al., 2018; Teanby, 2015; Teanby & Wookey, 2011). While the uncertainty on these detection estimates is large (ranging 0.1–30 per Earth year), the discrepancy between predictions and observations suggests that some of the assumptions relating to impact detectability require revision.

Because InSight is the only seismic station on Mars, its ability to constrain marsquake hypocenters is limited. Detection of an impact-generated seismic signal, whose location is determined by spacecraft images, would therefore be particularly valuable (Daubar et al., 2018). In the spring of 2019 one such small impact

(1.5 m crater diameter) occurred nearby (Daubar et al., 2020). Despite close proximity to the lander (~40 km), it could not be connected definitively with a specific seismic signal during the constrained time period. Predictions of the signal expected from this impact utilized various assumptions and scaling relationships relating crater size and seismic moment, which we test and improve upon in this work.

Seismic detectability estimates for small impacts on Mars make assumptions about the seismic moment and seismic efficiency (the proportion of the impact energy radiated as seismic waves) of impacts that are likely to occur during InSight's lifespan. However, neither quantity has been well constrained for impacts of relevant scale, primarily due to lack of observational and experimental data. Several scaling relationships relating seismic moment to impactor properties have been proposed (Gudkova et al., 2015; Lognonné et al., 2009; Shishkin, 2007; Teanby & Wookey, 2011), but their seismic moment predictions differ by more than an order of magnitude for small impacts (Daubar et al., 2018).

Seismic efficiency has been measured in laboratory-scale impact experiments (McGarr et al., 1969; Richardson & Kedar, 2013; Yasui et al., 2015), artificial or missile impact experiments on the Moon and Earth (Latham, Ewing, et al. 1970; Latham, McDonald, et al. 1970), in numerical simulations (Güldemeister & Wünnemann, 2017), and via theoretical scaling relationships (Lognonné et al., 2009; Shishkin, 2007). However, the resulting seismic efficiency estimates span 4 orders of magnitude (10^{-3} to 10^{-7}). This is likely due to variations in target and impactor properties, but a thorough understanding of their influence on seismic efficiency is lacking. Additionally, upscaling the results of small-scale laboratory experiments to the relevant momentum range is difficult. Teanby and Wookey (2011) suggested a reference seismic efficiency value for Mars of 2×10^{-5}, and used that to estimate the detectability of teleseismic impacts; more recent work has proposed a nominal value of 5×10^{-4} (Daubar et al., 2018; Teanby, 2015). Improved understanding of seismic moment and seismic efficiency would enhance impact detectability predictions on Mars and provide more robust initial conditions for seismic wave propagation modeling, and perhaps help explain the current lack of definitive impact detections from InSight.

Here we use the iSALE (impact Simplified Arbitrary Lagrangian Eulerian) shock physics code (Amsden et al., 1980; Collins et al., 2004; Wünnemann et al., 2006) to simulate vertical impacts onto Martian regolith in the size range of events expected during the InSight mission. For each simulation, we characterize the impact as a seismic source by calculating the scalar seismic moment and seismic efficiency. We also examine the anisotropy of the seismic moment tensor for vertical impacts and hence probe the analogy between impacts and underground explosions. Finally, we discuss our results in the context of the InSight mission and present revised estimates of the number of expected impact detections.

2. Theory

2.1. Scalar Seismic Moment

The seismic moment tensor describes the geometry and magnitude of a seismic source. It is often combined with a source-time function to define the source signal in seismic wave propagation modeling. Since the amplitude of the synthetic wave model is proportional to the seismic moment, synthetic seismograms generated for a given source-time function can be easily rescaled given the seismic moment.

The seismic moment tensor, M_{ij}, comprises three force dipoles (the diagonal components) and six force couples (the off-diagonal components). For a point source (a common approximation for explosions and impacts), the force couples can be neglected and M_{ij} simplifies to a diagonal tensor. For an isotropic point source the diagonal elements of the tensor are equal, $M_{ii} = M_1$. While a deeply buried explosion in a uniform medium is often treated as an isotropic point source, whether impacts can also be approximated as an isotropic seismic source is yet to be demonstrated.

2.2. Seismic Moment of a Buried Explosion

A simple expression for the scalar seismic moment of a buried explosion can be derived assuming equivalence between an explosive point source and three mutually perpendicular force dipoles acting in opposing directions parallel to the dipole (Müller, 1973). An explosive point source in an unbounded medium can be defined in terms of its displacement potential:

$$\phi(R, t) = \frac{F(t - R/c_P)}{R}, \tag{1}$$

where c_P is the P wave speed, R is the (spherical) radial distance from the source, t is time after the explosion, and $F(t)$ is the reduced displacement potential (Haskell, 1967; Müller, 1973; Shishkin, 2007). An equivalent radiation of seismic waves by three dipoles occurs if their moment function is

$$M_e(t) = -4\pi\rho c_P^2 F(t), \tag{2}$$

where ρ is the target density. The final value of this dipole moment function, $M_e(t)$, defines the scalar moment of the explosion M_1 (Müller, 1973; Shishkin, 2007):

$$M_1 = M_e(\infty) = -4\pi\rho c_P^2 F(\infty). \tag{3}$$

M_1 can be defined in terms of the average residual radial displacement $\langle D_1\rangle = -\langle F(\infty)\rangle/R_1^2$ at any distance $R_1 \geq R_e$, where R_e is the elastic radius at which plastic deformation stops and linear elasticity laws begin to hold. Taking S_1 as the surface area of a sphere of radius R_1 surrounding the explosion, M_1 can be expressed in terms of S_1, D_1, and the elastic moduli of the target:

$$M_1 = \rho c_P^2 S_1\langle D_1\rangle = \left(K + \frac{4G}{3}\right) S_1\langle D_1\rangle, \tag{4}$$

where K and G are the bulk and shear modulus of the target material, respectively. This implies that the seismic moment is proportional to the displaced volume $V_1 = S_1\langle D_1\rangle$ (Shishkin, 2007).

Considering stress as a function of radius from a buried explosion also allows the seismic moment to be defined in terms of the shear strength of the deformed ground σ_s and the volume of fractured (or plastically deformed) material $V_f = 4\pi R_e^3/3$ (Shishkin, 2007):

$$M_1 = \frac{4\pi}{3} R_e^3 \sigma_s \left(\frac{c_P}{c_S}\right)^2, \tag{5}$$

where c_S is the S wave speed. Equivalence between these definitions implies the following relationship between the residual displacement at the elastic limit and the ratio of shear strength to shear modulus:

$$\frac{\langle D_e\rangle}{R_e} \approx \frac{\sigma_s}{3G}. \tag{6}$$

The radiated seismic energy from a buried explosion E_s can be defined in a similar manner (Haskell, 1967) and expressed as a function of the work done to overcome the strength forces to produce the displaced volume:

$$E_s = b\sigma_s S_1\langle D_1\rangle, \tag{7}$$

where b is a constant that depends on the target material (Shishkin, 2007). Comparison of this equation with Equation 4 leads to

$$\frac{E_s}{M_1} = c\frac{\sigma_s}{G}, \tag{8}$$

where c is another material-dependent constant that is also expected to depend on the source mechanism.

2.3. Seismic Moment of an Impact

An impact differs from an explosion, as considered by Müller (1973), in that it occurs at the free-surface boundary of a half-space and is therefore spherically asymmetric (Shishkin, 2007). However, by analogy with a buried explosion the seismic moment of an impact should still depend on both the displaced volume (beyond the elastic limit), according to Equation 4, and the volume of permanently deformed material, according to Equation 5, provided the average R_e, the surface area S_1, and the average residual displacement $\langle D_1\rangle$ at this limit, are defined appropriately.

Walker (2003) presented an alternative definition for the seismic moment of a vertical impact: a force couple tensor, with the terms of the tensor given by a force multiplied by the couple distance. For an axially-symmetric wave, the horizontal force couple at the wave front is proportional to the change in horizontal momentum across the wave divided by the time of arrival (force) times the cylindrical wave front

radius r (distance). This implies that the horizontal moment should be approximately proportional to the horizontal momentum transfer times the wave speed. While this force couple can be defined for the two horizontal directions within the target, the presence of the free surface implies a vertical component for the moment cannot be defined similarly because the downward component of momentum is not balanced in the other direction as a force couple. Instead, Walker (2003) showed that by analogy with a spherically symmetric explosion, the horizontal seismic moment components $M_{rr} + M_{\theta\theta}$ can be defined as

$$M_{rr} + M_{\theta\theta} = \frac{1}{t} \int \rho v_r r \mathrm{d}V, \tag{9}$$

where v_r is the particle velocity in the radial (cylindrical geometry) direction, r is the (cylindrical) radial distance from the symmetry axis and t is time since the impact. For a spherically-symmetric explosion, the vertical moment M_{zz} can be defined similarly and the scalar moment $M_1 = M_{zz} = (M_{rr} + M_{\theta\theta})/2$, implying:

$$M_1 = \frac{1}{2}\frac{1}{t} \int \rho v_r r \mathrm{d}V. \tag{10}$$

Although there is no net horizontal momentum transferred in a vertical impact, owing to axial symmetry, horizontal motion is still imparted to the target. Walker (2003) also showed that in the absence of a definable vertical seismic moment M_{zz} for an impact, the sphericity (isotropy) of loading could be measured by the following term:

$$\gamma = \frac{M_{rr} + M_{\theta\theta}}{2 p_z c_P}, \tag{11}$$

where p_z is the vertical momentum transferred to the target. A sphericity of loading $\gamma > 1$, which Walker (2003) considers typical for impact loading, implies that more force is delivered in the outward, radial direction than is delivered vertically.

Assuming an impact-generated signal is similar to one generated by a point force density, Gudkova et al. (2015) proposed the vertical component of the seismic moment $M_{zz} = p_z c_P$, as another definition of the seismic moment of an impact. Extending the approach of Lognonné et al. (2009) and Gudkova et al. (2011) of defining the impact seismic source-time function, this model relates seismic scalar moment to impactor momentum via

$$M_1 = S p_i c_P, \tag{12}$$

where p_i is impactor momentum and S is an amplification factor to account for additional momentum imparted to the target by ejecta debris expelled from the growing crater. S depends on impact velocity as $S = 1 + \eta(v/1\,\mathrm{km/s})^{0.22}$. For a vertical impact, Sp_i is essentially the vertical momentum, p_z, transferred to the target during impact:

$$p_z = \int_{V_t} \rho v_z \mathrm{d}V, \tag{13}$$

where ρ is target density, v_z is vertical material velocity due to impact. V_t is the integration volume representing the target that is not ejected.

2.4. Seismic Efficiency of an Impact

A popular approximation for the energy radiated as seismic waves E_s from an impact (Güldemeister & Wünnemann, 2017; Schultz & Gault, 1975) assumes the seismic wave is symmetric across a hemispherical shell and calculates the seismic energy by integrating the power transferred to the target at radius R in the elastic domain over the duration of the wave pulse (Rinehart, 1960). Assuming a triangular wave pulse of pressure amplitude $P_{\max}$ and half-width Δt, E_s can be defined as

$$E_s = \frac{P_{\max}^2 \pi R^2 \Delta t}{3 \rho c_P}, \tag{14}$$

(Schultz & Gault, 1975). Seismic efficiency k_s can therefore be defined as the ratio of radiated to impact energy:

$$k_s = \frac{E_s}{E_i}. \tag{15}$$

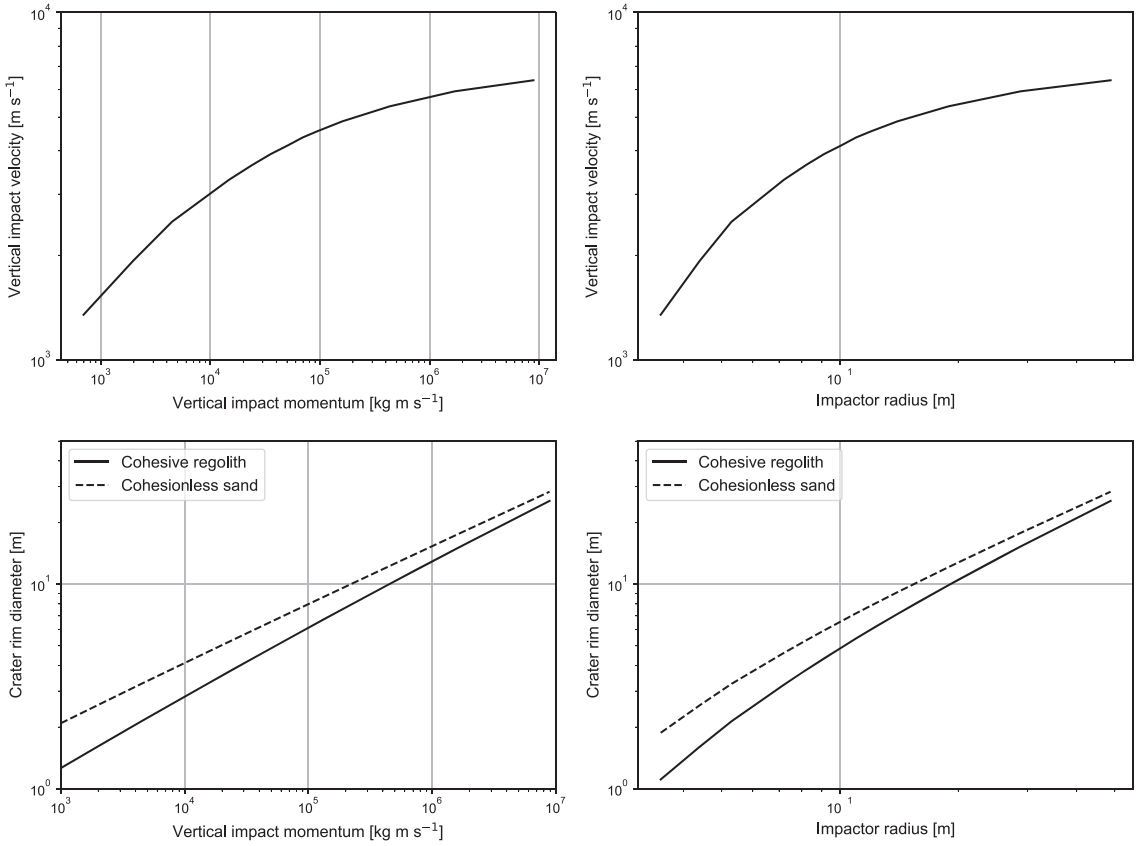

Figure 1. The expected crater size (bottom) and vertical component of the impact velocity (top) (for an atmospheric entry velocity of 10 km s^{-1}) are shown as a function of impactor radius (right) and vertical impact momentum (left). Crater rim diameter estimates used π group scaling (Holsapple, 1993) for cohesionless dry sand and for a porous cohesive regolith with a nominal strength $Y = 50$ kPa, with a target density of 1,590 kg m^{-3}, an impactor density of 2,860 kg m^{-3}, and a surface gravity 3.71 m s^{-2} (see section 3.2 for detailed material model justification). A 30% enlargement factor is applied to convert from preimpact-level to rim-level diameter and to account for rim collapse (Holsapple, 1993).

3. Methods

3.1. Approach

We used the iSALE shock physics code (Wünnemann et al., 2006) to simulate seismic wave generation by small impacts on Mars. iSALE is a finite-difference shock physics code based on the SALE hydrocode (Amsden et al., 1980) and adapted to simulate hypervelocity impact processes in planetary materials. Modifications to SALE include an elastoplastic constitutive model, fragmentation and strength models for dilatant geological materials (Collins, 2014; Collins et al., 2004; Ivanov et al., 1997; Melosh et al., 1992), various equations of state (EoS), and a porosity compaction model (Collins et al., 2011; Wünnemann et al., 2006).

In this first investigation of seismic signals generated by impacts on Mars we considered a range of typical impact scenarios likely to be detected by InSight, including the size range of the newly occurring nearby crater. Following prelanding impact detection estimates (Teanby, 2015) we focused on impacts most likely to be detected during the InSight mission: those that produce craters of diameter 1–30 m, which occur across Mars ~1,000–10 times per Earth year. Accounting for uncertainty in target strength (Daubar et al., 2020) and applying well-established impactor crater scaling equations (Holsapple, 1993), this corresponds to a range in vertical impactor momentum, radius, and mass of 10^3–10^7 kg m s^{-1}, 0.03–0.5 m, and 0.5–10^3 kg, respectively (Figure 1).

As the smallest impactors in this size range are likely to be substantially retarded by atmospheric entry, we chose the ground impact velocity and postablation mass for each impactor size by solving the standard equations of meteoroid entry dynamics (McMullan & Collins, 2019). These calculations assumed a preentry impactor speed of 10 km s^{-1}, the average impact speed on Mars (Le Feuvre & Wieczorek, 2011), an initial impact angle to the horizontal of 45° and an impactor density of 2,860 kg m^{-3} (to be consistent with

Table 1
Impactor Radius (r_i), Vertical Velocity (v_i), and Predicted Crater Diameters for Simulations in This Work

Simulation number	Impactor radius, r_i (m)	Vertical velocity, v_i (m s^{-1})	Rim diameter (sand, m)	Rim diameter (regolith, m)
1	0.035	1,350	1.88	1.11
2	0.044	1,930	2.56	1.60
3	0.053	2,500	3.26	2.14
4	0.072	3,300	4.61	3.22
5	0.082	3,640	5.31	3.80
6	0.091	3,910	5.93	4.33
7	0.10	4,150	6.60	4.90
8	0.11	4,370	7.21	5.43
9	0.12	4,550	7.85	6.00
10	0.14	4,860	9.13	7.15
11	0.19	5,370	12.1	9.89
12	0.29	5,930	17.8	15.3
13	0.49	6,380	28.3	25.5

our impactor material model, see section 3.2). We assume an initial impact angle of 45° to the horizontal in our atmospheric entry calculation because it is the most probable impact angle. However, to simulate seismic wave generation following ground impact we approximate the oblique impact as a vertical impact because vertical impacts are less computationally demanding, allowing us to track wave propagation much farther from the impact site than would otherwise be possible. To account for the difference in crater size between a vertical and oblique impact, we adopt the widely used convention of taking the vertical component of the oblique ground impact velocity as the impact speed in our vertical impact scenarios (Chapman & McKinnon, 1986; Elbeshausen et al., 2009). The expected crater size, vertical impact momentum, and vertical component of the impact velocity are shown as a function of impactor radius in Figure 1 and the impactor size, vertical impact speed at the ground, and crater size estimates are given in Table 1. Of the scenarios we consider, Scenarios 1 and 2 represent plausible candidates for the newly discovered crater on Mars (Daubar et al., 2020).

To simulate these vertical impacts we used a two-dimensional mesh in cylindrical ($r-z$) geometry. To capture the impact process and stress wave propagation from the moment of impact until the stress wave transitioned well into the elastic regime, a computational domain extending to >10 times the expected crater radius, >100 times the impactor radius, was required. In most simulations, the required mesh extended 3,000 cells in both horizontal and vertical directions, affording an impactor resolution of 10 cells per projectile radius (cppr). Therefore, for a 4.4 cm impactor radius (Model 2 in Table 1), the cell size was 4.4 mm and the simulation domain extended to 13.2 m across and 13.2 m below the surface. This spatial resolution has proven adequate previously to accurately capture stress wave decay for determining seismic efficiency (Güldemeister & Wünnemann, 2017). To diagnose the propagation and decay of the impact-generated stress wave, the state of field variables in the mesh was saved at regular time intervals. To gain a higher temporal resolution record of wave propagation at specific points in the target material, Lagrangian probes were placed radially away from impact point (Figure 2). In particular, probes measured residual displacement for use in seismic moment calculations; and pressure-time pulse amplitude and width for use in seismic energy and efficiency calculations.

Particularly challenging in this work was tracking accurately the shock wave as it decayed in amplitude by 6 orders of magnitude into a very weak stress wave that induced displacements as small as 2×10^{-4} impactor radii. Therefore, in most simulations we neglected gravitational acceleration and hence the effect of overburden pressure. In iSALE's standard implementation, including gravity requires the construction of an initial vertical pressure (and density) gradient in the target that balances the gravitational acceleration to a prescribed tolerance. However, even a small, unavoidable imbalance can lead to nonphysical stress waves that, while very low amplitude, are sufficient to contaminate the far-field wave field and prevent accurate tracking of the impact wave to long distances.

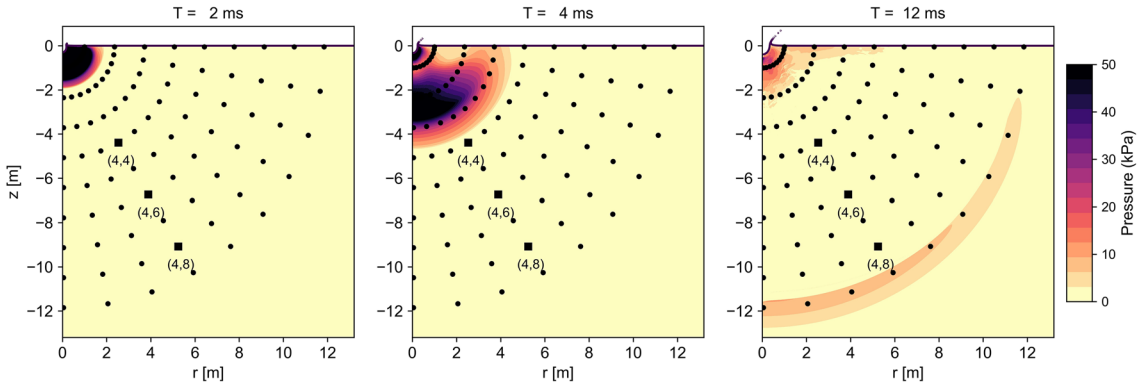

Figure 2. (left to right) Three snapshots of impact-generated stress wave as it traverses the simulation mesh for a nominal vertical impact of a 1-kg basalt projectile striking the target at 1.93 km/s. Markers indicate locations of Lagrangian probes acting as virtual seismometers. Properties of the three probes highlighted by black squares are shown in more detail in later sections.

We note that the total number of cells in the simulation mesh we employ renders the time taken to fully simulate the crater formation unreasonably long. We therefore rely on crater scaling relationships (Holsapple, 1993) to determine the final crater size. This approach is justified because previous work has demonstrated very good agreement between these scaling relationships and the results of iSALE vertical impact simulations in a range of target materials (Prieur et al., 2017; Raducan et al., 2019; Wünnemann et al., 2006, 2016).

3.2. Material Models

In all simulations, the impactor was represented as a nonporous basalt sphere of density 2,860 kg m^{-3} and a nominal rock-like strength (Britt & Consolmagno, 2003). Because the impact speeds we considered are rather low and do not necessitate a complex multiphase equation of state, we used computationally fast analytical Tillotson equation of state (Tillotson, 1962) to describe the impactor's volumetric response. Other than the reference density and bulk modulus, we expect our simulation results to be insensitive to the exact equation of state and strength model used to represent the impactor material (see Table S1 in the supporting information). Figure 3 compares the Hugoniot curve defined by this equation of state and shock wave data for nonporous basalt. The impactor's deviatoric strength was described using a simple pressure-dependent strength model (Lundborg, 1968) (Table 2).

The generation and propagation of seismic signals from an impact is likely to be sensitive to the nature of the Martian surface at that location. Since the purpose of this work is to provide a baseline assessment of the seismic efficiency and moment of small impacts on Mars within hundreds of kilometers of InSight, we consider a highly simplified target material model broadly representative of the upper tens of meters of Mars near the lander. This shallow depth is most relevant because seismic waves from such nearby impacts will not penetrate deeper into Mars. Our results should therefore provide a general reference frame on which future site-specific investigations at other locations with different geology can build.

Remote sensing, geological mapping, and analysis of InSight observations (Golombek et al., 2017, 2020; Morgan et al., 2018; Warner et al., 2017) show that beneath a thin surficial layer of dust and sand is a layer of duricrust of variable thickness (≤10 cm) and a cohesion of a few to tens of kPa. This is underlain by a regolith of poorly sorted, unconsolidated sand and rocks (Golombek et al., 2020). Beneath the landing site, the fine-grained, high-porosity impact generated regolith is ~2 m thick (Lognonné et al., 2020) and is presumed (based on ejecta observations from nearby craters and a nearby scarp exposing a section of the subsurface) to grade with depth first into coarse, blocky ejecta and then over meters to tens of meters into fractured basalt flows (Golombek et al., 2017; Warner et al., 2017).

Seismic wave generation and near-field propagation will be most sensitive to changes in porosity, density, and seismic velocity with depth. Initial seismic velocity estimates based on direct travel time measurement of HP^3 mole hammering signals, and analysis of ground compliance, suggest a two-layer near-surface structure beneath the lander (Lognonné et al., 2020). The ~2 m thick upper regolith has *P* wave velocity ~120 m s^{-1} and is underlain by a higher-impedance layer with *P* wave velocity in the range 500–1,500 m s^{-1} (Lognonné et al., 2020). For the meter- to decameter-scale impact craters of interest here, the wave

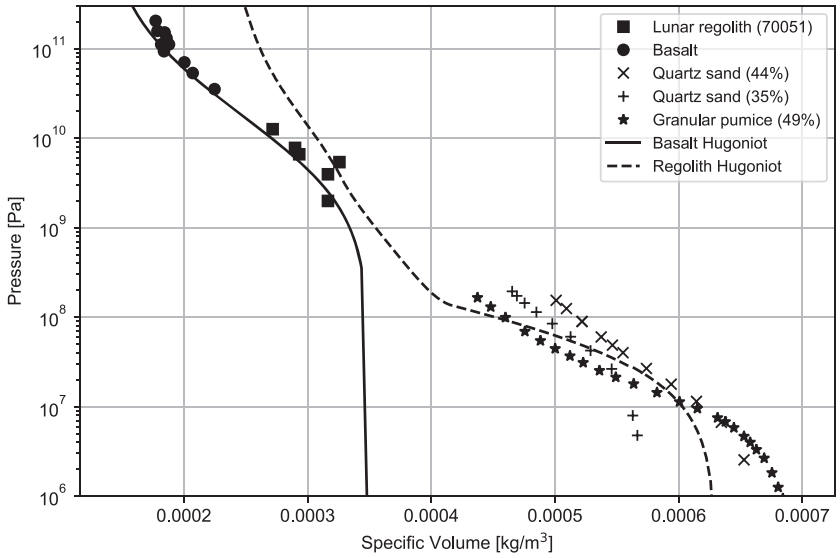

Figure 3. Hugoniot curves in pressure-specific volume space used to represent nonporous basalt impactor (solid line) and regolith target material (dashed line). Symbols show experimental shock (solid symbols) and crush (open symbols) data for analog materials for comparison. The porosity of the granular analog materials is given in parentheses. Shock Hugoniot data from Ahrens and Cole (1974) and van Thiel (1977); crush curve data from Housen et al. (2018) and Luo et al. (2011).

generation region will be predominantly in the lower of these two layers. We therefore adopt a one-layer target material model with a bulk density ($\rho = 1589\,\mathrm{kg\,m^{-3}}$), bulk porosity ($\phi = 44\%$), bulk sound speed ($c_B = 857\,\mathrm{m\,s^{-1}}$), and P wave speed ($c_P = 1088\,\mathrm{m\,s^{-1}}$) that is likely representative of the upper tens of meters of Mars near InSight. For simulations 1–3 with crater diameter ≤2 m (similar to the newly formed 1.5 m crater near InSight), a material model with elastic moduli and seismic velocities closer to those of the shallowest subsurface would be the more appropriate. However, as the plastic and shock response of the target material is relatively insensitive to these material parameters, we expect that the important nonlinear near-field effects, such as pore collapse and shear failure, are well described by our material model. In the interest of consistency, we therefore use the same target properties for all impact simulations, although we

Table 2
Impactor and Target Material Properties

Material model parameter	Symbol	Impactor	Target
Reference density (kg m^{-3})	ρ_0	2,860	1,589
Bulk sound speed (m s^{-1})	c_B	2,598	857
Initial distension	α_0	1	1.8
Initial porosity	ϕ_0	0	0.44
Bulk modulus (GPa)	K_0	19.3	1.17
Shear modulus (GPa)	G_0	8.9	0.54
Poisson ratio	ν	0.3	0.3
Internal friction coefficient	μ	0.7	0.6
Limiting strength (GPa)	Y_m	1	0.25
Cohesion (kPa)	Y_0	5	5
Elastic compaction threshold	ϵ_e	—	-2×10^{-4}
Transition distention	α_x	—	1.2
Exp. compaction rate	κ	—	0.98
Sounds speed ratio	χ	—	0.33

Note. Descriptions of material model parameters can be found in Collins et al. (2004, 2011) and Wünnemann et al. (2006).

acknowledge that these properties are most oversimplified for the three smallest impact scenarios. Although we refer to this material here as regolith, we emphasize that this material model approximates the bulk target stratigraphy from fine-grained regolith, through coarse ejecta to fractured basalt and not just the upper layer. We describe the target material strength with a simple pressure-dependent strength model (Lundborg, 1968) with a shear strength of 5 kPa at zero pressure, an internal friction coefficient of 0.6 (approximately equivalent to a friction angle of 37° and a high-pressure shear strength limit of 250 MPa (Table 2). The $\epsilon - \alpha$ compaction model parameters that describe the crush behavior of the target material were determined based on comparison of the Hugoniot curve of our simulated target material with crush data of analog target materials (granular pumice and quartz sand) and shock wave data for lunar regolith (Figure 3). We consider the sensitivity of our results to small variations in the crush curve of the target model; however, we reserve a detailed study of the influence of target property variations on seismic moment and efficiency for future work.

3.3. Seismic Source Characterization

The seismic source signature of our simulated impacts was characterized in simulation data postprocessing. Next, we describe this methodology using the scenario of a 1-kg impactor striking the surface at 1.93 km/s.

3.3.1. Seismic Moment

We employed three scalar seismic moment calculation approaches, based on Equations 4, (10), and (12). First, based on the analogy between an impact and an explosion, the scalar moment was calculated at a given radial distance from the impact point using the residual radial displacement:

$$M_{1M}(R) = \left(K + \frac{4G}{3}\right) S(R)\langle D_R(R)\rangle, \tag{16}$$

where K and G are the (reference) bulk and shear moduli of the target material, respectively, $S(R) = 2\pi R^2$ is the surface area of a hemisphere of radius R, centered at the impact point, and $\langle D_R(R)\rangle$ is the average residual radial displacement of target material at radius R. To calculate $\langle D_R(R,\theta)\rangle$ we used an array of Lagrangian probes (Figure 2) which recorded displacement as a function of time with maximum temporal resolution equal to the simulation time step. Supporting Information S1 details further how residual displacement was derived.

In the second method, the seismic moment in the horizontal direction was calculated following Walker (2003):

$$M_{rW}(t) = \frac{1}{2t}\sum_{i}^{n} \rho[i]\bar{v}_r[i]V[i], \tag{17}$$

where t is time after impact, $\rho[i]$ is material density in cell i, $V[i]$ is volume in cell i, and $\bar{v}_r[i]$ is average (horizontal) radial velocity in cell i. Summation is over all n cells in the mesh, below the preimpact target surface level; cells above the preimpact surface were excluded, removing ejected material from the seismic moment calculation. $M_{rW}(t)$ was evaluated at the regular time intervals, at which mesh data were saved.

In the third approach, we calculated the vertical seismic moment as

$$M_{zGL} = c_P p_z = c_P \sum_{i}^{n} \rho[i]\bar{v}_z[i]V[i], \tag{18}$$

where this summation is over the same target cells as above; $\bar{v}_z[i]$ is the average vertical velocity in cell i.

For the example simulation, plotting $M_{zGL}(t)$ and $M_{rW}(t)$ as a function of wave front radius $R = c_P t$ for comparison with $M_{1M}(R)$ shows that each measure of the seismic moment converges at ~8 m (Figure 4) as the wave transitions from plastic to elastic deformation. The seismic moment derived from residual displacement at radius R, $M_{1M}(R)$, converges to the true scalar seismic moment from above; the other two estimates of seismic moment converge to their final values from below (Figure 4).

Because the $M_{rW}(t)$ moment converges at a radial distance between the other moments, we used the M_{rW} convergence distance as a proxy for the elastic radius R_e. As $M_{rW}(R)$ is an average moment over all polar angles at R, our estimate of R_e is also an average over all polar angles and we therefore assume a hemispherical geometry for the elastic limit. On the other hand, the fact that the vertical moment M_{zGL} converges at a smaller radius than the horizontal moment suggests that the elastic radius may in fact be smaller in the

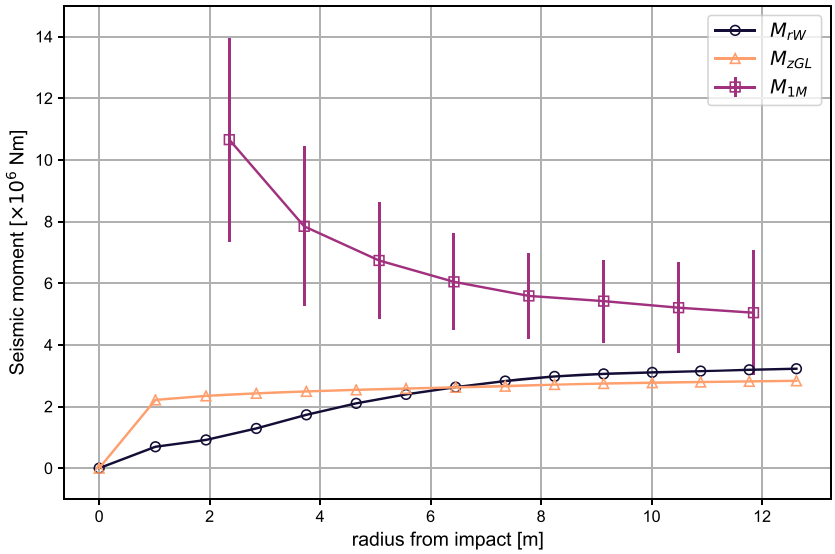

Figure 4. Three seismic scalar moment estimates as a function of radius from impact for a nominal model of a 1-kg impactor striking the target at 1.93 km/s.

vertical direction than in the horizontal. Such a geometry is consistent with the inferred extent of fracturing at Meteor crater, for example, but is inconsistent with the deep and narrow geometry of the elastic limit assumed by Shishkin (2007).

To verify our moment-based proxy for the elastic radius for the example impact we compared radial displacement-time paths recorded by probes at different radii from the impact (see Text S2). The normalized displacement time paths are self-similar in the elastic region, as expected. Hence, in all further simulations we used this proxy to approximately delimit the elastic region and derived the scalar seismic moment of the impact for each method by averaging values of each moment in the elastic region ($R > R_e$).

The three estimates of the scalar seismic moment are consistent within a factor of 2. M_{zGL} and M_{rW} are close to being within the uncertainty in M_{1M} that is attributed to the polar variation in residual radial displacement. The difference between M_{1M} and the other two estimates is likely due to oversimplification of our assumption that the fracture surface (elastic limit) is hemispherical. The M_{rW} to M_{zGL} ratio, γ, is only slightly greater than one, implying an almost isotropic P wave source for vertical impacts. Further investigation is needed to determine to what extent this result can be extended to oblique impacts, which are known to result in much higher$S$ to P wave amplitude ratios than near-vertical impacts (Lognonné et al., 2009).

The vertical momentum transferred to the target p_z, calculated in the process of determining M_{zGL} can also be used to determine S, the amplification factor describing the vertical momentum transfer enhancement of the ejecta:

$$S = \frac{p_z}{p_i} = \frac{M_{zGL}}{c_P}, \tag{19}$$

where p_i is impactor momentum. For the example simulation, $S \approx 1.3$ implying a 30% enhancement of momentum transfer from ejecta, consistent with the semiempirical approximation of Lognonné et al. (2009). Note, however, that the calculated values of S, p_z, and M_{zGL} are sensitive to the approach used to exclude ejected momentum from the integral of momentum density over the target. For simplicity, we assume all material above the preimpact level is ejecta. Moving this threshold altitude up or down by one impactor radius changes p_z and its dependencies by ~15%.

3.3.2. Seismic Energy and Seismic Efficiency

To calculate the energy radiated from the impact as seismic waves E_s, closely following Güldemeister and Wünnemann (2017), we employed the triangular pulse approximation (Equation 14), to estimate the time integral of the power transferred to the target by the passage of the stress wave at each Lagrangian probe (Figure 2). When applying Equation 14 $P_{\max}$ is defined as the peak pressure recorded by the probe, Δt is the full width at half maximum of the pressure pulse, R is the (spherical) impactor probe radial distance; ρ and

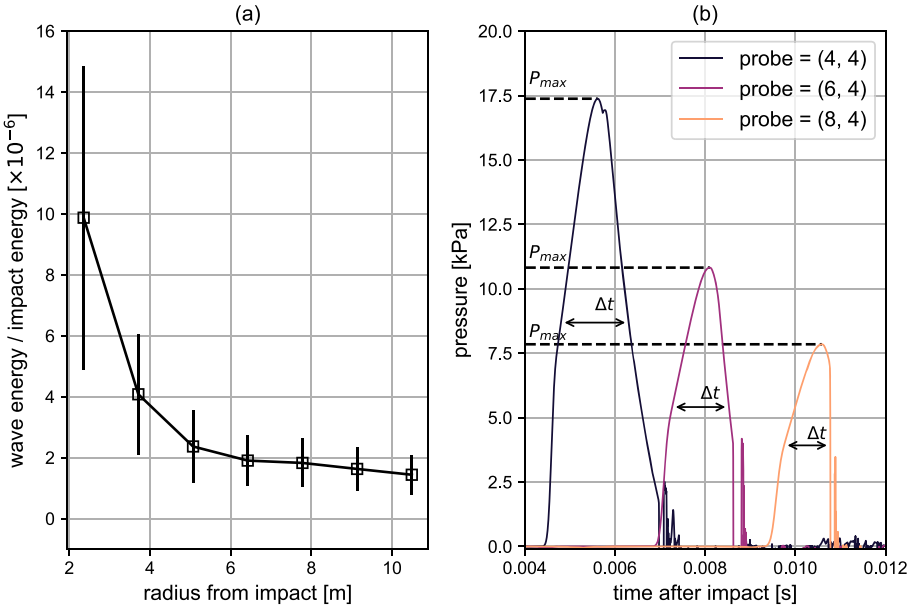

Figure 5. (a) Ratio of wave energy and impact energy as a function of radius from impact for a nominal model of a 1-kg impactor striking the surface at 1.93 km/s. (b) Pressure recorded as a function of time by three probes highlighted in Figure 2. Black dashed lines mark peak pressure values used in Equation 14 and the half-width, dt, of each trace is also marked.

c_P are the reference density and P wave speed of the pristine target material, respectively. Three example pressure traces are shown in Figure 5b, including peak pressures and half widths.

To calculate wave energy at each radius R, wave properties were measured for each probe at that radius and averaged across polar angles, weighted by the area of the hemisphere spanned by that angle. Calculated this way, wave energy converges at $\sim R_e$. Hence, to calculate the radiated seismic energy and seismic efficiency with this approach, we defined E_s as the average E_W at probes with $R > R_e$, and k_s as E_s/E_i. Although the energy losses are greatest in the first 2 m from the impact site, the elastic radius in the target extends well beyond the crater rim.

4. Results

Our simulation results characterize impacts as a seismic source for the range in impactor momentum expected to be typical of impacts that might be detected by InSight. Table 3 documents the various characteristics of the seismic source for each impact scenario.

4.1. Scalar Seismic Moment

Our simulations show that each estimate of the scalar seismic moment is linearly proportional to impact momentum (Figure 6). $M_{1M} \approx 2 \times M_{rW}$ for all impact momenta. This difference can be partially attributed to the polar variation of residual radial displacement. All data, including respective errors, were combined to produce a single data set. Using a least squares regression, a best fit relationship between seismic scalar moment M_1 (Nm) and impact momentum p_i (kg m s^{-1}) is

$$M_1 = 10^{3.18\pm0.08} p_i^{1.02\pm0.01}. \quad (20)$$

Pearson's R value for this relationship is 0.997, indicating good data fit.

Values calculated from our simulations agree very closely with the theoretical GL model (Figure 6). For the purposes of this comparison, in the GL model we assumed $\eta = 0.3$, as adopted in Daubar et al. (2018) and Lognonné et al. (2009).

The results for Simulations 1 and 2 are 9.6×10^5 to 5.2×10^6 Nm. This is toward the lower end of the values estimated for the newly observed crater near InSight using scaling laws in Daubar et al. (2020): 10^6 to 10^7 Nm.

Table 3
Complete Results for All Models

Simulation	p_i (kg m s^{-1})	E_i (J)	M_{rW} (Nm)	M_{1M} (Nm)	M_{zGL} (Nm)	S	γ	k_s	E_s (J)	$R_e(r_i)$
1	7.00×10^{2}	4.73×10^{5}	1.09×10^{6}	1.86×10^{6}	9.61×10^{5}	1.26	1.14	1.97×10^{-6}	0.93	182
2	1.99×10^{3}	1.92×10^{6}	3.19×10^{6}	5.22×10^{6}	2.81×10^{6}	1.30	1.13	1.63×10^{-6}	3.13	200
3	4.50×10^{3}	5.63×10^{6}	7.18×10^{6}	1.00×10^{7}	6.39×10^{6}	1.31	1.12	1.40×10^{-6}	7.87	185
4	1.49×10^{4}	2.46×10^{7}	2.51×10^{7}	4.01×10^{7}	2.28×10^{7}	1.41	1.10	1.26×10^{-6}	30.85	209
5	2.43×10^{4}	4.42×10^{7}	4.08×10^{7}	6.68×10^{7}	3.74×10^{7}	1.42	1.09	1.18×10^{-6}	52.2	208
6	3.56×10^{4}	6.97×10^{7}	6.08×10^{7}	9.08×10^{7}	5.57×10^{7}	1.44	1.09	1.13×10^{-6}	78.6	216
7	5.17×10^{4}	1.07×10^{8}	8.67×10^{7}	1.45×10^{8}	7.94×10^{7}	1.41	1.09	1.00×10^{-6}	109	236
8	7.03×10^{4}	1.54×10^{8}	1.22×10^{8}	1.97×10^{8}	1.12×10^{8}	1.46	1.09	1.10×10^{-6}	168	242
9	9.51×10^{4}	2.16×10^{8}	1.66×10^{8}	2.79×10^{8}	1.52×10^{8}	1.47	1.09	9.64×10^{-7}	209	240
10	1.61×10^{5}	3.92×10^{8}	2.85×10^{8}	3.6×10^{8}	2.63×10^{8}	1.50	1.08	9.42×10^{-7}	369	222
11	4.45×10^{5}	1.20×10^{9}	7.74×10^{8}	1.32×10^{9}	7.33×10^{8}	1.51	1.06	8.75×10^{-7}	1,050	224
12	1.75×10^{6}	5.19×10^{9}	3.17×10^{9}	5.28×10^{9}	2.94×10^{9}	1.54	1.08	8.26×10^{-7}	4,290	245
13	9.08×10^{6}	2.9×10^{10}	1.65×10^{10}	2.66×10^{10}	1.54×10^{10}	1.56	1.07	9.24×10^{-7}	26,800	242

This suggests that the detectability of this crater is likely to have been near the lower bound considered by Daubar et al. (2020).

M_{zGL} is proportional to the vertical momentum transferred to the target by the impact (Gudkova et al., 2015; Lognonné et al., 2009). Previous work has shown that momentum transfer to the ground is amplified by material ejected from the crater (McGarr et al., 1969), with amplification extent dependent on impactor and target properties (Holsapple, 2004; Raducan et al., 2019). The amplification is characterized by the ejecta amplification factor S. NB in many previous studies, β is used to denote the ejecta amplification factor. S is used here for consistency with the GL model (Lognonné et al., 2009). For the small impacts on Mars simulated here, S increases with impact momentum from 1.25 to 1.6 (Table 3). These values are comparable to amplification factors derived from ejecta scaling relationships and used in previous estimates of the impulse applied to the ground by impacts (Lognonné et al., 2009).

The ratio of the horizontal to vertical seismic moment components provides a measure of source sphericalness. For our simulation results, γ, calculated as the ratio of M_{rW} to M_{zGL} (Equation 11) was 1.05–1.15, implying an approximately isotropic seismic moment tensor for vertical impacts. The vertical component of

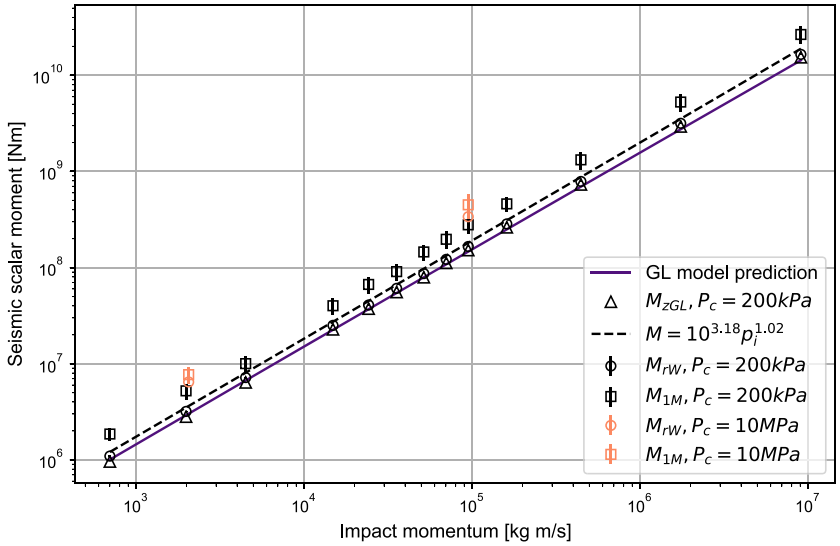

Figure 6. Three scalar seismic moment estimates for all simulations as a function of impactor momentum. Solid line: GL model seismic moment prediction, assuming $\eta = 0.3$ (following Lognonné et al., 2009) and $c_P = 1088$ m s^{-1} (consistent with our target material model).

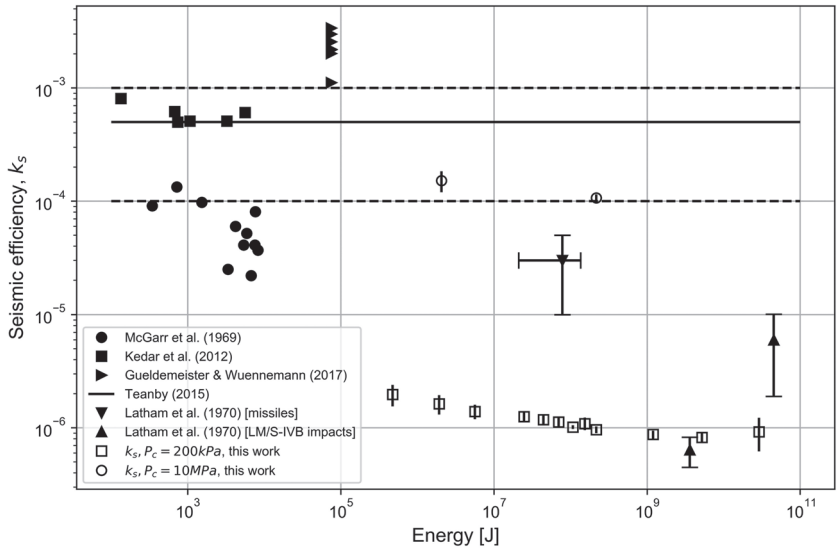

Figure 7. Seismic efficiency as a function of impact energy. Our results fall between 8×10^{-7} and 2×10^{-6}, ≈2 orders of magnitude below prelanding predictions. To illustrate the sensitivity of seismic efficiency to the crush curve parameters, a result for a simulation using crushing strength of 10 MPa is also shown at 1–2 $\times 10^{-4}$. (Note that the vertical bars on the results represent the error bars, for some simulation smaller than the size of the marker.) Data obtained in previous studies, numerical (Güldemeister & Wünnemann, 2017) and experimental (Latham, Ewing, et al. 1970; Latham, McDonald, et al., 1970; McGarr et al., 1969; Richardson & Kedar, 2013), are also presented (see Acknowledgments for data tables).

the moment tensor is only 5–15% smaller than each of the radial components. Higher momentum impacts exhibited lower values of γ but a higher S, so were more isotropic while more momentum was being imparted to the ground. Because the simulations in this work were restricted to vertical impacts, future work should explore if these results extend to oblique impacts.

Based on convergence of M_{rW}, the average radius of the plastic-elastic regime transition over all polar angles, R_e, increased with impact momentum from $R_e \approx$ 180–240 impactor radii (Table 3). This corresponds to 7–11 crater radii, depending on crater scaling assumptions (Figure 1). This is substantially larger than the elastic radius equal to the crater radius assumed in the analytical model of seismic wave generation of Shishkin (2007); and suggested by observations of terrestrial craters (Ackermann et al., 1975; Smith et al., 1999), which found the fracture radius of ~2–2.5 crater radii. We attribute this difference to the difference in strength between target material used in our simulations (~5 kPa) and typical terrestrial rocks (~10 MPa). For the very weak material in our simulations, the wave must decay to a lower amplitude, which occurs at a further distance. Hence, this estimate will vary for craters formed in areas with different target properties than in our simulations. Additionally, the elastic radius determined in our work may be overestimated, due to the absence of overburden pressure in our simulations. If the characteristic timescale of seismic wave generation is the time taken for the impact stress wave to reach the elastic radius (Gudkova et al., 2015), this implies a wave generation timescale ≈10 R_c/c_P, where R_c is crater radius and c_P is P wave velocity.

4.2. Seismic Efficiency

The seismic efficiencies of our simulated impacts are at the low end of previous estimates (Figure 7). They are substantially lower than seismic efficiencies measured in laboratory-scale impact experiments in sand (McGarr et al., 1969; Richardson & Kedar, 2013) and that based on missile impacts on Earth (Latham, McDonald, et al. 1970). Our values are comparable to estimates based on large-scale artificial impacts on the Moon (Latham, Ewing, et al. 1970), which represent good analogs to our simulations in terms of impactor momentum and energy, and target properties. However, we acknowledge that the impactors in the artificial lunar impacts were low density, easily crushed, metal spacecraft, which are poor analogs to strong, rocky meteorites used in our simulations. Further research is necessary to determine the effect of individual impactor properties on seismic efficiency.

Our simulations reveal the seismic efficiency of small impacts is also much smaller than estimates produced in laboratory experiments of impacts in porous rocks and iSALE simulations of those experiments (Güldemeister & Wünnemann, 2017). We attribute the difference in k_s between this work and that of (Güldemeister & Wünnemann, 2017), which used a similar modeling approach, to the dramatically different properties of assumed target material, in particular the effective crushing strength $p_c \approx -K_0\epsilon_e$. Here, the Martian soil was represented with a crushing strength (the onset of permanent compaction) of ~200 kPa, based on the crushing behavior of analog materials (Figure 3); the rock targets of Güldemeister and Wünnemann (2017) were represented with a crushing strength of ~700 MPa.

To assess our simulation results' sensitivity to details of the target material crush curve we performed additional simulations with different $\epsilon - \alpha$ model parameters. To achieve an effective crushing strength of ~10 MPa we increased the value of ϵ_e to -1×10^{-2}, and kept other parameters in Table 2 the same. For those models, more appropriate for a soft rock, the seismic efficiency was 2 orders of magnitude larger (Figure 7). Seismic moment in those simulations was only 3× larger. While a more thorough investigation of the effect of target crushing strength and other material properties on seismic efficiency is required, this suggests that the detectability of small impacts on Mars might be very sensitive to the proximity to the surface of dense, strong, and high impedance materials.

Our seismic efficiency values decrease slightly with increasing impact energy and impact velocity. This likely reflects the fact that at higher impact speeds more energy is partitioned into waste heat.

5. Implications for Detectability of Impacts by InSight

Our simulation results show a linear relationship between impact momentum and seismic moment (and therefore ground motion amplitude). We now use this result to re-evaluate InSight prelanding impact detectability estimates.

The expected number of detectable impacts has been estimated in several ways (Daubar et al., 2015, 2018; Lognonné & Johnson, 2015; Teanby & Wookey, 2011; Teanby, 2015). Teanby and Wookey (2011) estimated detectable impact numbers by combining seismic wave form modeling, observed cratering rates and an empirical relationship between crater size and seismic moment (Figure 8a). This empirical scaling relationship relies on three elements: an empirical relationship between crater size and impact energy, based largely on terrestrial explosion data (Figure 8b); the seismic efficiency of the impact; and a relationship between radiated seismic energy and seismic moment, based on small earthquake and nuclear explosion data (Figure 8c). Our simulation results provide an independent test of these elements.

The radiated seismic energy E_s and scalar seismic moment M_1 determined from our simulations is fit well by a linear relationship with a constant of proportionality of 1×10^{-6}. Assuming $\sigma_s = 5$ kPa and $G = 0.54$ GPa, this implies that for impacts the constant c in Equation 8 is ≈0.1, which is lower than commonly assumed for earthquakes (0.54) and explosions (0.27) (Shishkin, 2007). When combined with earthquake and explosion data, our simulation results follow a power law trend akin to the Teanby and Wookey (2011) model (TW2011, hereafter). In the most relevant range of seismic energy (1×10^5 J) the seismic moment predicted by the TW2011 model is 2–3 times that predicted by our simulations (Figure 8c). To convert between seismic energy and impact energy, TW2011 adopted a seismic efficiency of $k_s = 2 \times 10^{-5}$, ~20 times higher than determined here for the weak, porous surface of Mars near InSight. When combined with the difference in $E_s - M$ scaling, this results in TW2011 overestimating seismic moment by a factor of 40–60 for the same size crater.

Although the relationship between impact energy and crater size was not explicitly tested by our iSALE simulations, previous work has shown consistency between the π group scaling of crater diameter used here and iSALE simulations of crater formation in regolith-like targets (Prieur et al., 2017; Raducan et al., 2019). For the impactor parameters adopted here, which account approximately for deceleration during atmospheric entry, the scaling relationship between crater size and impact energy used in TW2011 agrees reasonably with our results for craters of diameter >10 m, but overestimates the impact energy required to produce smaller craters by up to an order of magnitude (Figure 8b).

When all components of the crater size to seismic moment scaling relationship are combined, TW2011 predicts a seismic moment 1–2 orders of magnitude higher for a given crater size than our results. We attribute this difference to a combination of the low seismic efficiency of impacts into very weak porous regolith

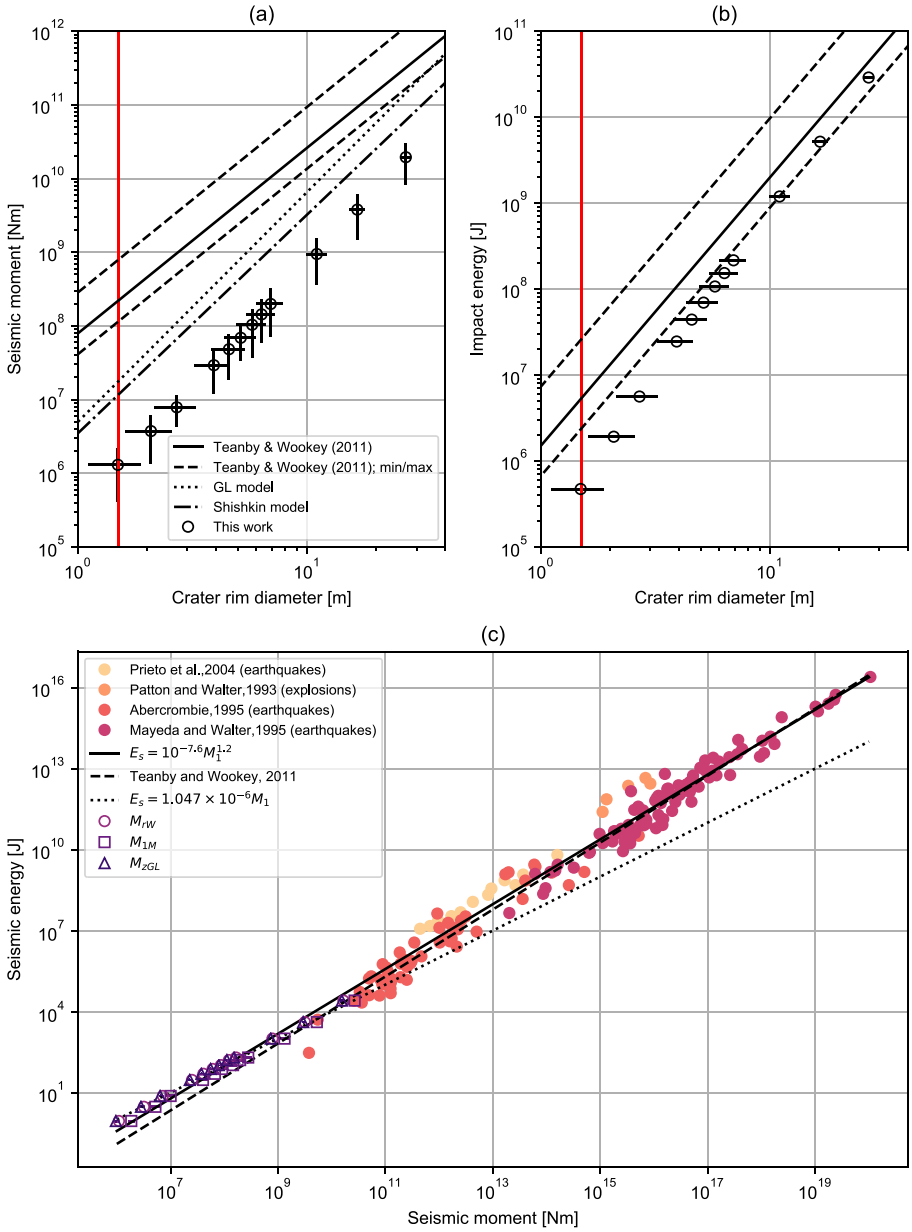

Figure 8. Scalar seismic moment (a) and impact energy (b) as a function of crater rim diameter. Simulation results of seismic moment and assumed impact energy are compared to the scaling relationships developed by Teanby and Wookey (2011), Gudkova et al. (2011, 2015) (GL model), and Shishkin (2007) (Shishkin model). Note that the latter two models include correction factors to account for transmission of seismic energy from regolith into bedrock (Daubar et al., 2018) and incorporate both strength- and gravity-dominated scaling relationships of Holsapple (1993) to determine crater size. Horizontal error bars indicate the range of predicted crater diameter according to π group scaling; vertical error bars represent the range in seismic moment estimates from this work. Red vertical lines in (a) and (b) mark the size of the newly discovered small crater near InSight. (c) Seismic moment versus seismic energy, alongside data from previous studies of earthquakes and nuclear explosions (see Acknowledgments for data tables).

shown by our results and the previous work's extrapolation of experimental data based on impact energy as opposed to impact momentum. As discussed in Daubar et al. (2018) an important consideration for reconciling these disparate estimates of seismic moment is the effect of target material properties and transmission of seismic energy into bedrock underlying the impacted material. Also shown in Figure 8a are estimates of seismic moment versus crater rim diameter derived using the GL model and the Shishkin model (as described by Daubar et al., 2018) that include a total bedrock moment correction factor of ≈ 5 to account for the effect of a typical crustal bedrock ($c_P = 1{,}000\ \mathrm{m\ s^{-1}}$, $\rho = 2{,}700\ \mathrm{kg\ m^{-3}}$) underlying soft impacted regolith

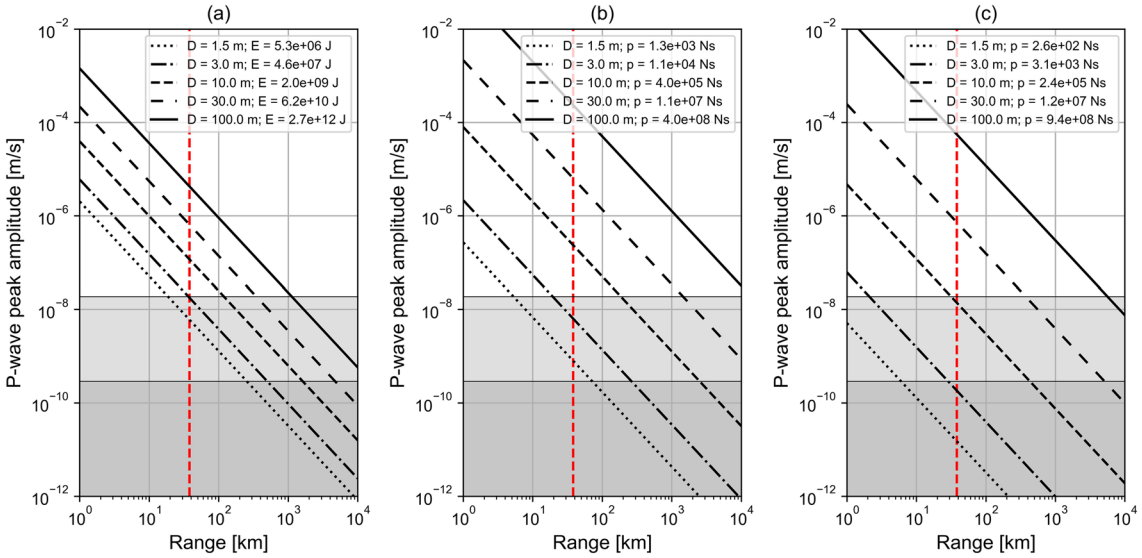

Figure 9. Predictions of *P* wave peak amplitude versus range for different impact crater diameters using three different scaling approaches. (a) *P* wave amplitude is scaled by the square root of the impact energy as described by Teanby (2015); crater diameter is related to impact energy by the scaling relationship of Teanby and Wookey (2011). (b) *P* wave amplitude as measured in terrestrial missile impacts (Latham, McDonald, et al., 1970) is scaled by the impactor momentum, crater diameter is related to impactor momentum by π group scaling (Holsapple, 1993) for a cohesive soil (see Equation 22). The results presented assume $v_\perp = 3{,}535\,\mathrm{m\,s^{-1}}$, $Y = 50\,\mathrm{kPa}$, $\rho = 1{,}500\,\mathrm{kg\,m^{-3}}$, $\delta = 2{,}000\,\mathrm{kg\,m^{-3}}$. (c) *P* wave amplitude as measured in lunar SIVB impacts (Latham, McDonald, et al., 1970) is scaled by the impactor momentum, crater diameter is related to impactor momentum by π group scaling (Holsapple, 1993) for cohesionless sand (see Equation 21). The results presented assume the same parameters as (b) although cohesion is neglected. Horizontal lines and shading represent measured InSight noise levels at 1–16 Hz from Lognonné et al. (2019, 2020) under low-noise and high-noise conditions. Red vertical lines mark the 38-km distance corresponding to the small newly discovered crater on Mars. The impact energy E or momentum p corresponding to each crater size is given in the legend.

($c_P = 330\,\mathrm{m\,s^{-1}}$, $\rho = 1{,}500\,\mathrm{kg\,m^{-3}}$). These lie between our simulation estimates in a regolith analog that do not include a bedrock correction and those of TW2011, based in part on data from explosions and impacts directly into bedrock.

For a nominal noise model, Teanby and Wookey (2011) estimated a total impact-generated seismicity of 10^{13} to 10^{14} Nm per Earth year, and one detectable teleseismic range impact every 10 years. Based on the much lower seismic moments predicted by this work, the TW2011 predictions at the lower end of their estimates seem the most likely. These imply a total impact-generated seismicity of 10^{11} to 10^{13} Nm and an average recurrence interval of over 100 years for a detectable teleseismic range impact.

To better constrain the detectability of smaller impacts, more proximal to InSight, Teanby (2015) adopted an empirical approach to directly relate impact energy to ground velocity amplitude, based on data from impact and explosions experiments. This approach also employed the crater size to impact energy relationship from Teanby and Wookey (2011) so also likely represents an overly optimistic estimate of impact detections.

Our numerical simulations advocate a momentum-based approach for extrapolating from ground truth impact scenarios to small impact scenarios on Mars. We therefore modified the approach of Teanby (2015) to develop two empirical relationships between *P* wave peak amplitude v, range x, and crater size D, based on vertical impactor momentum, rather than impact energy; one for impacts into a dry cohesionless sand and one for impacts into a more robust and strong soil (Figure 9). These relationships use π group scaling equations to relate impactor momentum (and other properties) to crater size (Daubar et al., 2020) combined with separate fits to ground motion versus range data.

For cohesionless sand, using a fit to seismic data from the artificial impact of the Saturn IV boosters on the lunar regolith (Latham, Ewing, et al. 1970):

$$v(x,D) = 1.59\times10^{-9}\xi_2 x^{-1.6}D^3$$
$$\xi_2 = \left(\frac{v_i}{1{,}000\,\mathrm{m\,s^{-1}}}\right)^{-0.23}\left(\frac{g}{3.71\,\mathrm{m\,s^{-2}}}\right)^{0.61}\left(\frac{\delta}{2{,}000\,\mathrm{kg\,m^{-3}}}\right)^{-0.19}\left(\frac{\rho}{1{,}500\,\mathrm{kg\,m^{-3}}}\right)^{1.19} \quad (21)$$

where g is gravity in m s^{-2}. This scaling relationship is based on data from impact experiments in a similar target material to that employed in our simulations and that showed a similarly low seismic efficiency and therefore may be most appropriate for surfaces on Mars similar to the InSight landing site.

For a cohesive soil, using a fit to seismic data from terrestrial missile impacts (Teanby, 2015)

$$v(x,D) = 1.64\times10^{-7}\xi_1 x^{-1.6}D^{3.6}$$
$$\xi_1 = \left(\frac{v_i}{1{,}000\,\mathrm{m\,s^{-1}}}\right)^{-0.23}\left(\frac{Y}{100\,\mathrm{kPa}}\right)^{0.62}\left(\frac{\delta}{2{,}000\,\mathrm{kg\,m^{-3}}}\right)^{-0.2}\left(\frac{\rho}{1{,}500\,\mathrm{kg\,m^{-3}}}\right)^{0.59} \quad (22)$$

where x is the range in km, D is crater rim diameter in m, $v_\perp$ is vertical impact velocity in m s^{-1}, Y is the cohesion of the soil in kPa, and δ and ρ are the impactor and target density, respectively, in SI units. This scaling relationship is based on data from impact experiments in a stronger target material than employed in our simulations and that showed a much higher seismic efficiency and therefore may be more appropriate for impacts in regions of Mars covered with denser, more cohesive surface materials.

The two momentum-based empirical scaling relationships (Figures 9b and 9c) show a much greater variation in peak amplitude with crater diameter than the original energy-based approach (Figure 9a). For a ~30-m crater diameter, which represents the scenario closest to the Saturn IV booster impacts on the lunar regolith, the three approaches are relatively consistent, differing by only a factor of 5. However, when crater size and ground velocity is scaled by impactor momentum the peak amplitudes predicted for craters less than a few meters in diameter are 10 to 1,000 times lower than the energy-scaling predictions, depending on the material properties of the target. Additionally, for the 1.5 m crater known to have occurred near InSight (Daubar et al., 2020), the detailed wave propagation modeling predicted amplitudes of 10^{-8} m/s using seismic scalar moment of 10^7 Nm, which is ≈10 times higher than our simulation results. Momentum-scaling approach produces amplitudes between ≈10^{-9} m/s (for an impact into cohesive regolith) and ≈10^{-11} m/s (for an impact into cohesionless sand). The large differences between these scaling relationships imply that even a single seismically detected impact would provide invaluable insight into impact-generated seismic waves and the local geology by constraining the material properties at the impact site.

The measured noise at the InSight landing site varies significantly over the course of a day. Following Daubar et al. (2020) and Teanby (2015) we consider seismic noise in the 1–16 Hz frequency range as being most appropriate for small impact craters. The measured seismic noise at the 4 Hz geometric center of the range varies from $p_a = 1.5\times10^{-9}$ m s^{-2} Hz$^{-1/2}$ during quiet periods to 1×10^{-7} m s^{-2} Hz$^{-1/2}$ during noisy periods (Lognonné et al., 2019, 2020). This corresponds to peak noise levels in seismic ground velocity of $n_v = 2.9\times10^{-10}$ m s^{-1} to 1.9×10^{-8} m s^{-1}, using $n_v = (5/8\pi)p_a\sqrt{1/f_1 - 1/f_2}$ from Teanby (2015) for a frequency range of $f_1 = 1$ Hz to $f_2 = 16$ Hz (horizontal lines in Figure 9). Our momentum-based scaling approach suggests that craters of diameter <10 m are detectable at much shorter range from InSight than previously proposed. In the most pessimistic case, where the impact occurs in a loose, porous, and cohesionless target, a 1.5-m crater >5 km away would be undetectable (consistent with conclusions of Daubar et al., 2020), even under low-noise conditions. A 3-m crater would only be detectable if it occurred within 2 km. On the other hand, this approach suggests that craters of diameter >10 m are much more detectable, particularly if the impact were to occur in a part of Mars with a stronger, denser surface with more efficient ground coupling of impactor momentum. Such events offer the best chance of detection within hundreds of km of InSight and are a possibility: a 10 m diameter crater has a one in two chance of occurring within 300 km in a Martian year using the Hartmann (2005) production function or a one in five chance using the Daubar et al. (2013) production function.

To predict seismic moment from crater size, future studies should avoid using the highly uncertain seismic efficiency. Instead, we recommend a momentum-based approach whereby the impactor momentum is first determined from crater size using π group scaling and then seismic moment is calculated from impactor momentum using Equation 20. For typical small impacts on Mars, the relationship between seismic moment and crater diameter found here (Figure 8a) can be used as a first approximation:

$$M = 3.5\times10^5\left(\frac{D}{1\,\mathrm{m}}\right)^{3.3}\ \mathrm{Nm}. \quad (23)$$

For impacts into targets that differ substantially from the homogeneous representative target model employed here, some amplitude correction may be necessary to account for the transmission/reflection of seismic energy between the impacted target material and the bedrock below (Daubar et al., 2018).

6. Conclusions

To characterize the seismic signal generated by typical small impacts on Mars, we simulated a set of small impacts onto Martian regolith using the iSALE shock physics code. For each simulation, we characterized the impact as a seismic source using scalar seismic moment, seismic efficiency, ejecta momentum amplification factor, sphericalness of loading, and the radius of plastic-elastic wave transition.

Three approaches for calculating the scalar seismic moment of an impact from numerical simulation data (Lognonné et al., 2009; Müller, 1973; Walker, 2003) produced values that agree to within a factor of 2 and show that scalar seismic moment scales almost linearly with impact momentum. Future studies should use either a horizontal or vertical seismic moment approach: they produce consistent results and obviate the need for Lagrangian probes. Additionally, M_{zGL} required a shorter simulation to converge, hence this approach may be preferred if computational resources are limited.

For small impacts, the ratio of transferred momentum to impactor momentum increases from 1.3 for a 1-m crater to 1.6 for a 30-m crater, indicating a small but significant momentum amplification from ejecta. The leading impact-generated stress wave transitioned from a plastic to elastic behavior at ~10 crater radii. Moreover, the ratio of the horizontal to vertical seismic moment components is ~1, implying, for vertical impacts at least, that small impacts on Mars are well represented by an isotropic seismic moment tensor. However, further work is required to determine whether this extends to oblique impacts.

The seismic efficiency (the ratio of radiated seismic energy to impact energy) of our simulated impacts was $\sim 1 \times 10^{-6}$, decreasing with impact velocity. This is akin to seismic efficiencies determined from artificial lunar impacts, but substantially smaller than estimates from terrestrial missile impacts and laboratory impact experiments. Seismic efficiency was very sensitive to the crushing curve of the target material. In particular, a factor of 50 increase in crushing strength increased seismic efficiency by about 2 orders of magnitude, while seismic moment only tripled. Due in part to this sensitivity, seismic moment is a more robust way to characterize the seismic source than seismic energy.

Our simulation-based estimates of the seismic moment of small impacts on Mars are lower than prelanding estimates, while our seismic efficiency results are 1 to 2 orders of magnitude below the value assumed in some prelanding estimates of the seismic detectability of small impacts by InSight (Daubar et al., 2018; Teanby & Wookey, 2011). Thus, impacts producing craters of diameter <10 m are less seismically detectable than previously thought, perhaps explaining InSight's lack of detections to date. A >10 m crater formed within 400 km of InSight offers the most promising chance of detection.

Data Availability Statement

Supporting information (including model input files and literature data used in fugures) can be found in Wójcicka (2020) (https://doi.org/10.5281/zenodo.3862698).

Acknowledgments
N. W. and G. S. C.'s research is funded by the UK Space Agency (Grants ST/S001514/1 and ST/T002026/1). K. M.'s research is fully funded by the Australian Government through the ARC (DE180100584, DP180100661). I. J. D.'s research is supported by NASA InSight Participating Scientist Grant 80NSSC20K0971. N. A. T. is funded by UK Space Agency Grants ST/R002096/1 and ST/T002972/1. We gratefully acknowledge the developers of iSALE (www.isale-code.de). This is InSight contribution number 135. Two reviewers and Editor Laurent Montesi provided helpful comments that improved the manuscript.

References

Ackermann, H. D., Godson, R. H., & Watkins, J. S. (1975). A seismic refraction technique used for subsurface investigations at Meteor Crater, Arizona. *Journal of Geophysical Research*, *80*, 765–775. https://doi.org/10.1029/jb080i005p00765

Ahrens, T. J., & Cole, D. M. (1974). Shock Shock compression and adiabatic release of lunar fines from Apollo 17. Proceedings of the Fifth Lunar Conference (Vol. 3).

Amsden, A. A., Ruppel, H. M., & Hirt, C. W. (1980). SALE: A Simplified ALE computer program for fluid flow at all speeds. Los Alamos National Laboratories Report (Vol. LA-8095). Los Alamos, NM (United States). https://doi.org/10.2172/5176006

Banerdt, W. B., Smrekar, S. E., Banfield, D., Giardini, D., Golombek, M., Johnson, C. L., et al. (2020). Initial results from the InSight mission on Mars. *Nature Geoscience*, *13*(3), 183–189. https://doi.org/10.1038/s41561-020-0544-y

Britt, D. T., & Consolmagno, G. J. S. J. (2003). Stony meteorite porosities and densities: A review of the data through 2001. *Meteoritics & Planetary Science*, *38*(8), 1161–1180. https://doi.org/10.1111/j.1945-5100.2003.tb00305.x

Chapman, C. R., & McKinnon, W. B. (1986). Cratering of planetary satellites. In *Satellites* (pp. 492–580).

Collins, G. S. (2014). Numerical simulations of impact crater formation with dilatancy. *Journal of Geophysical Research: Planets*, *119*, 2600–2619. https://doi.org/10.1002/2014JE004708

Collins, G. S., Melosh, H. J., & Ivanov, B. A. (2004). Modeling damage and deformation in impact simulations. *Meteoritics & Planetary Science*, *39*(2), 217–231. https://doi.org/10.1002/2014JE004708

Collins, G. S., Melosh, H. J., & Wünnemann, K. (2011). Improvements to the α porous compaction model for simulating impacts into high-porosity solar system objects. *International Journal of Impact Engineering*, *38*(6), 434–439. https://doi.org/10.1016/j.ijimpeng.2010.10.013

Daubar, I. J., Golombek, M. P., McEwen Byrne, S., Kreslavsky, M., Schmerr, N. C., et al. (2015). Measurement of the Current Martian Cratering Size Frequency Distribution, Predictions for and Expected Improvements from InSight. In *Lunar and Planetary Science Conference 46* (p. 2468).

Daubar, I. J., Lognonné, P., Teanby, N. A., Miljkovic, K., Stevanović, J., Vaubaillon, J., et al. (2018). Impact-seismic investigations of the InSight mission. *Space Science Reviews*, *214*(8), 132. https://doi.org/10.1007/s11214-018-0562-x

Daubar, I. J., Lognonné, P., Teanby, N., & Collins, G. (2020). A new crater near InSight: Implications for seismic impact detectability on Mars. *Journal of Geophysical Research: Planets*, *125*, e2020JE006382. https://doi.org/10.1029/2020JE006382

Daubar, I. J., McEwen, A. S., Byrne, S., Kennedy, M. R., & Ivanov, B. (2013). The current Martian cratering rate. *Icarus*, *225*(1), 506–516. https://doi.org/10.1016/J.ICARUS.2013.04.009

Elbeshausen, D., Wünnemann, K., & Collins, G. S. (2009). Scaling of oblique impacts in frictional targets: Implications for crater size and formation mechanisms. *Icarus*, *204*(2), 716–731. https://doi.org/10.1016/j.icarus.2009.07.018

Güldemeister, N., & Wünnemann, K. (2017). Quantitative analysis of impact-induced seismic signals by numerical modeling. *Icarus*, *296*, 15–27. https://doi.org/10.1016/J.ICARUS.2017.05.010

Giardini, D., Lognonné, P., Banerdt, W. B., Pike, W., Christensen, U., Ceylan, S., et al. (2020). The seismicity of Mars. *Nature Geoscience*, *13*, 205–212. https://doi.org/10.1038/s41561-020-0539-8

Golombek, M., Kipp, D., Warner, N., Daubar, I. J., Fergason, R., Kirk, R. L., et al. (2017). Selection of the InSight landing site. *Space Science Reviews*, *211*(1–4), 5–95. https://doi.org/10.1007/s11214-016-0321-9

Golombek, M., Warner, N. H., Grant, J. A., Hauber, E., Ansan, V., Weitz, C. M., et al. (2020). Geology of the InSight landing site on Mars. *Nature Communications*, *11*(1), 1014. https://doi.org/10.1038/s41467-020-14679-1

Gudkova, T. V., Lognonné, P., & Gagnepain-Beyneix, J. (2011). Large impacts detected by the Apollo seismometers: Impactor mass and source cutoff frequency estimations. *Icarus*, *211*(2), 1049–1065. https://doi.org/10.1016/J.ICARUS.2010.10.028

Gudkova, T. V., Lognonné, P., Miljković, K., & Gagnepain-Beyneix, J. (2015). Impact cutoff frequency momentum scaling law inverted from Apollo seismic data. *Earth and Planetary Science Letters*, *427*, 57–65. https://doi.org/10.1016/J.EPSL.2015.06.037

Hartmann, W. K. (2005). Martian cratering 8: Isochron refinement and the chronology of Mars. *Icarus*, *174*(2 SPEC. ISS.), 294–320. https://doi.org/10.1016/j.icarus.2004.11.023

Haskell, N. A. (1967). Analytic approximation for the elastic radiation from a contained underground explosion. *Journal of Geophysical Research*, *72*(10), 2583–2587. https://doi.org/10.1029/jz072i010p02583

Holsapple, K. A. (1993). The scaling of impact processes in planetary sciences. *Annual Review of Earth and Planetary Sciences*, *21*(1), 333–373. https://doi.org/10.1146/annurev.ea.21.050193.002001

Holsapple, K. A. (2004). About deflecting asteroids and comets. In *Mitigation of Hazardous Comets and Asteroids* (M. J. S. Belton, T. H. Morgan, N. H. Samarasinha, & D. K. Yeomans, Eds.), pp. 113.

Housen, K. R., Sweet, W. J., & Holsapple, K. A. (2018). Impacts into porous asteroids. *Icarus*, *300*, 72–96. https://doi.org/10.1016/j.icarus.2017.08.019

Ivanov, B. A., Deniem, D., & Neukum, G. (1997). Implementation of dynamic strength models into 2D hydrocodes: Applications for atmospheric breakup and impact cratering. *International Journal of Impact Engineering*, *20*(1–5), 411–430. https://doi.org/10.1016/S0734-743X(97)87511-2

Latham, G., Ewing, M., Dorman, J., Press, F., Toksoz, N., Sutton, G., et al. (1970). Seismic data from man-made impacts on the Moon. *Science*, *170*(3958), 620–626. https://doi.org/10.1126/science.170.3958.620

Latham, G., McDonald, W. G., & Moore, H. J. (1970). Missile impacts as sources of seismic energy on the Moon. *Science*, *168*(3928), 242–245.

Le Feuvre, M., & Wieczorek, M. A. (2011). Nonuniform cratering of the Moon and a revised crater chronology of the inner solar system. *Icarus*, *214*(1), 1–20. https://doi.org/10.1016/J.ICARUS.2011.03.010

Lognonné, P., Banerdt, W. B., Giardini, D., Pike, W. T., Christensen, U., Laudet, P., et al. (2019). SEIS: Insight's seismic experiment for internal structure of Mars. *Space Science Reviews*, *215*(1), 12. https://doi.org/10.1007/s11214-018-0574-6

Lognonné, P., Banerdt, W. B., Pike, W. T., Giardini, D., Christensen, U., Garcia, R. F., et al. (2020). Constraints on the shallow elastic and anelastic structure of Mars from InSight seismic data. *Nature Geoscience*, *13*, 213–220. https://doi.org/10.1038/s41561-020-0536-y

Lognonné, P., & Johnson, C. L. (2015). Planetary seismology. *Treatise on geophysics: Second edition* (Vol. 10, pp. 65–120). Amsterdam: Elsevier Inc.

Lognonné, P., Le Feuvre, M., Johnson, C. L., & Weber, R. C. (2009). Moon meteoritic seismic hum: Steady state prediction. *Journal of Geophysical Research*, *114*, E12003. https://doi.org/10.1029/2008JE003294

Lundborg, N. (1968). Strength of rock-like materials. *International Journal of Rock Mechanics and Mining Sciences and*, *5*(5), 427–454. https://doi.org/10.1016/0148-9062(68)90046-6

Luo, H., Lu, H., Cooper, W. L., & Komanduri, R. (2011). Effect of mass density on the compressive behavior of dry sand under confinement at high strain rates. *Experimental Mechanics*, *51*(9), 1499–1510. https://doi.org/10.1007/s11340-011-9475-2

Müller, G. (1973). Seismic moment and long-period radiation of underground nuclear explosions. *Bulletin of the Seismological Society of America*, *63*(3), 847–857.

McGarr, A., Latham, G. V., & Gault, D. E. (1969). Meteoroid impacts as sources of seismicity on the Moon. *Journal of Geophysical Research*, *74*(25), 5981–5994. https://doi.org/10.1029/JB074i025p05981

McMullan, S., & Collins, G. S. (2019). Uncertainty quantification in continuous fragmentation airburst models. *Icarus*, *327*, 19–35. https://doi.org/10.1016/j.icarus.2019.02.013

Melosh, H. J., Ryan, E. V., & Asphaug, E. (1992). Dynamic fragmentation in impacts: Hydrocode simulation of laboratory impacts. *Journal of Geophysical Research*, *97*(E9), 14,735–14,759. https://doi.org/10.1029/92je01632

Morgan, P., Grott, M., Knapmeyer-Endrun, B., Golombek, M., Delage, P., Lognonné, P., et al. (2018). A pre-landing assessment of regolith properties at the InSight landing site. *Space Science Reviews*, *214*(6), 104.

Prieur, N. C., Rolf, T., Luther, R., Wünnemann, K., Xiao, Z., & Werner, S. C. (2017). The effect of target properties on transient crater scaling for simple craters. *Journal of Geophysical Research: Planets*, *122*, 1704–1726. https://doi.org/10.1002/2017JE005283

Raducan, S. D., Davison, T. M., Luther, R., & Collins, G. S. (2019). The role of asteroid strength, porosity and internal friction in impact momentum transfer. *Icarus*, *329*, 282–295. https://doi.org/10.1016/j.icarus.2019.03.040

Richardson, J. E., & Kedar, S. (2013). An experimental investigation of the seismic signal produced by hypervelocity impacts. In *Lunar and Planetary Science Conference 44*, abstract 2863.

Rinehart, J. S. (1960). On fractures caused by explosions and impacts. Quarterly of the Colorado School of Mines, Colorado School of Mines, 55 (4).

Schultz, P. H., & Gault, D. E. (1975). Seismic effects from major basin formations on the Moon and Mercury. *The Moon*, *12*(2), 159–177. https://doi.org/10.1007/BF00577875

Shishkin, N. I. (2007). Seismic efficiency of a contact explosion and a high-velocity impact. *Journal of Applied Mechanics and Technical Physics*, *48*(2), 145–152. https://doi.org/10.1007/s10808-007-0019-6

Smith, S. K., Grieve, R. A. F., Harris, J. R., & Singhroy, V. (1999). The utilization of RADARSAT-1 imagery for the characterization of terrestrial impact landforms. *Canadian Journal of Remote Sensing*, *25*(3), 218–228. https://doi.org/10.1080/07038992.1999.10874721

Teanby, N. A. (2015). Predicted detection rates of regional-scale meteorite impacts on Mars with the InSight short-period seismometer. *Icarus*, *256*, 49–62. https://doi.org/10.1016/J.ICARUS.2015.04.012

Teanby, N. A., & Wookey, J. (2011). Seismic detection of meteorite impacts on Mars. *Physics of the Earth and Planetary Interiors*, *186*(1–2), 70–80. https://doi.org/10.1016/J.PEPI.2011.03.004

Tillotson, J. H. (1962). Metallic equations of state for hypervelocity impacts. Report No. GA-3216, General Atomic, San Diego, CA, 43.

van Thiel, M. (1977). *Compedium of shock wave data*. Livermore: Lawrence Livermore Laboratory Report UCRL-50108.

Wünnemann, K., Collins, G. S., & Melosh, H. J. (2006). A strain-based porosity model for use in hydrocode simulations of impacts and implications for transient crater growth in porous targets. *Icarus*, *180*(2), 514–527. https://doi.org/10.1016/J.ICARUS.2005.10.013

Wünnemann, K., Zhu, M.-H., & Stöffler, D. (2016). Impacts into quartz sand: Crater formation, shock metamorphism, and ejecta distribution in laboratory experiments and numerical models. *Meteoritics & Planetary Science*, *51*(10), 1762–1794. https://doi.org/10.1111/maps.12710

Walker, J. D. (2003). Loading sources for seismological investigation of asteroids and comets. *International Journal of Impact Engineering*, *29*(1–10), 757–769. https://doi.org/10.1016/J.IJIMPENG.2003.10.022

Warner, N. H., Golombek, M. P., Sweeney, J., Fergason, R., Kirk, R., & Schwartz, C. (2017). Near surface stratigraphy and regolith production in Southwestern Elysium Planitia, Mars: Implications for Hesperian-Amazonian terrains and the InSight lander mission. *Space Science Reviews*, *211*(1–4), 147–190. https://doi.org/10.1007/s11214-017-0352-x

Wojcicka, N. (2020). nwojcicka/impact-seismic-source: impact-seismic-source (Version v1.0.2). Zenodo. http://doi.org/10.5281/zenodo.3974183

Yasui, M., Matsumoto, E., & Arakawa, M. (2015). Experimental study on impact-induced seismic wave propagation through granular materials. *Icarus*, *260*, 320–331. https://doi.org/10.1016/J.ICARUS.2015.07.032